

CaV₆O₁₆·2.8H₂O with Ca²⁺ Pillar and Water Lubrication as a High-Rate and Long-Life Cathode Material for Ca-Ion Batteries

Junjun Wang, Jianxiang Wang, Yalong Jiang, Fangyu Xiong, Shuangshuang Tan, Fan Qiao, Jinghui Chen, Qinyou An,* and Liqiang Mai*

Due to the low cost and low redox potential of calcium, calcium ion batteries (CIBs) are considered a competitive candidate for large-scale energy storage systems and have attracted increasing attention in recent years. However, the development of CIBs is still in its infancy and hindered by the lack of high-performance cathode materials. Herein, the metahewettite layered vanadium oxide with the Ca²⁺ pillar and water lubrication is reported as a cathode material for CIBs. Benefiting from the large interlayer spacing, pillar, and water lubrication effect, the as-prepared CaV₆O₁₆·2.8H₂O (CVO) delivers a high discharge capacity of 175.2 mAh g⁻¹ at 50 °C and 131.7 mAh g⁻¹ at room temperature, a long cycle life of 1000 cycles and the highest rate performance (up to 1000 mA g⁻¹) in organic electrolyte. Furthermore, a single-phase Ca²⁺ insertion and extraction reaction is revealed by in situ X-ray diffraction and in-situ Fourier transform infrared spectroscopy. Density functional theory computations indicate that Ca²⁺ tends to diffuse along the *b* direction with a low energy barrier of 0.36 eV in CVO. This work is bringing the performance of cathode materials for CIBs to a higher level and of great significance for accelerating the development of CIBs.

multivalent carriers can transfer multiple electrons, multivalent-ion batteries as potential candidates for post-LIBs are expected to achieve higher energy density. Among multivalent-ion (Mg²⁺, Ca²⁺, Zn²⁺, and Al³⁺) batteries, calcium ion batteries (CIBs) have received increasing attention in recent years due to the smallest polarization force of Ca²⁺ and the lowest redox potential of Ca (−2.87 V versus SHE), which means that CIBs may have better rate performance and higher working voltage.^[2,3] In addition, the reserves of Ca in the earth's crust are abundant, and Ca tends to plate/strip with dendrite-free morphology.^[4] Therefore, CIBs have the potential to become energy storage devices with low-cost, safety, and high energy density.^[5,6]

Recent breakthroughs in electrolytes and anode materials have greatly promoted the development of CIBs. For example, Zhao-Karger^[7] and Nazar^[8] suc-

1. Introduction

Due to the uneven distribution and scarcity of lithium in the earth's crust and the energy density of lithium-ion batteries (LIBs) based on insertion chemistry being close to the theoretical limit,^[1] the development of alternative electrochemical energy storage systems with high safety, long cycle life, low cost, and high energy density is of great significance. Since

cessively exploited the Ca[B(hfip)₄]₂-based electrolytes with compatibility with Ca metal at room temperature and high stability, which is important for the development of CIBs with high working voltage. Cheng, Pyo, and Kang reported tin foil^[9] and graphite^[10,11] as anode materials for CIBs, which will help promote the commercial application of CIBs. However, the cathode materials, as an important part of CIBs, still show poor electrochemical performance, which severely impedes the development of CIBs. The reported cathode materials for CIBs mainly include Prussian blue analogs,^[12,13] polyanionic salts,^[3,14–16] and layered transition metal oxygen or sulfides.^[17–19] Among these cathode materials, the layered vanadium oxides exhibit high Ca²⁺ storage capacity owing to their large interlayer spacing and the multivalent advantages of vanadium. However, due to the large radius and two charges of Ca²⁺, the layered structure of vanadium oxides is easily destroyed during Ca²⁺ insertion and deinsertion, resulting in poor cycling performance. Thus, it is important to find an effective strategy to stabilize the layered structure of vanadium oxides. Due to the pillar effect, pre-intercalation chemistry has been shown to be a good method to stabilize the structure of layered vanadium oxides.^[20] Our group reported that the pre-intercalation of Mg²⁺ and H₂O molecules between the layers of V₂O₅ can effectively improve the cycling

J. Wang, J. Wang, Y. Jiang, F. Xiong, S. Tan, F. Qiao, J. Chen, Q. An, L. Mai
State Key Laboratory of Advanced Technology for Materials Synthesis
and Processing

Wuhan University of Technology
Wuhan 430070, China

E-mail: anqinyou86@whut.edu.cn; mlq518@whut.edu.cn

Q. An, L. Mai

Foshan Xianhu Laboratory of the Advanced Energy Science and
Technology Guangdong Laboratory
Xianhu Hydrogen Valley
Foshan 528200, China

 The ORCID identification number(s) for the author(s) of this article can be found under <https://doi.org/10.1002/adfm.202113030>.

DOI: 10.1002/adfm.202113030

stability of V_2O_5 as cathode material for CIBs.^[21] However, the introduced Mg^{2+} will make the valence of V less than +5 and occupy some active sites, which causes $Mg_{0.25}V_2O_5 \cdot H_2O$ to exhibit low Ca^{2+} storage capacity. Therefore, the layered vanadium oxides with V^{5+} and metal ion pillared could be promising cathode materials for excellent performance CIBs.

Here, we report the $CaV_6O_{16} \cdot 2.8H_2O$ (CVO) with Ca^{2+} pillar and V^{5+} as a cathode material for CIBs. Benefiting from the large interlayer spacing, pillar, and water lubrication effect, CVO shows a discharge capacity of 175.2 mAh g^{-1} at 50 °C and 131.7 mAh g^{-1} at room temperature, the highest rate performance, and ultra-long cycle life of 1000 cycles in the $Ca(TFSI)_2$ /diethylene glycol dimethyl ether (G2). Furthermore, a battery with $CaV_6O_{16} \cdot 2.8H_2O$ as cathode material and Ca metal as an anode was assembled for the first time to verify the feasibility of layered vanadium oxides in Ca metal batteries. The Ca^{2+} storage mechanism and structural evolution of CVO were deeply studied by in situ X-ray diffraction (XRD), in situ Fourier

transform infrared spectroscopy (FTIR), and ex situ X-ray photoelectron spectrum (XPS). Density functional theory (DFT) computations were used to analyze the migration path of Ca^{2+} in CVO and corresponding energy barriers.

2. Result and Discussion

The CVO was synthesized by hydrothermal method with α - V_2O_5 and $Ca(OH)_2$ as starting materials. **Figure 1a** shows the schematic diagram of the formation and crystal structure of CVO. In the crystal structure of α - V_2O_5 , the layered structure is only composed of $[VO_5]$ square pyramid, and there are no ions and molecules between the layers. After structural reconstruction, the layered structure consists of $[VO_5]$ square pyramid and $[VO_6]$ octahedron. In addition, the insertion of Ca^{2+} and H_2O in the interlayers can enlarge the interlayer spacing of vanadium oxide (from 4.37 to 8.10 Å) and stabilize the layered

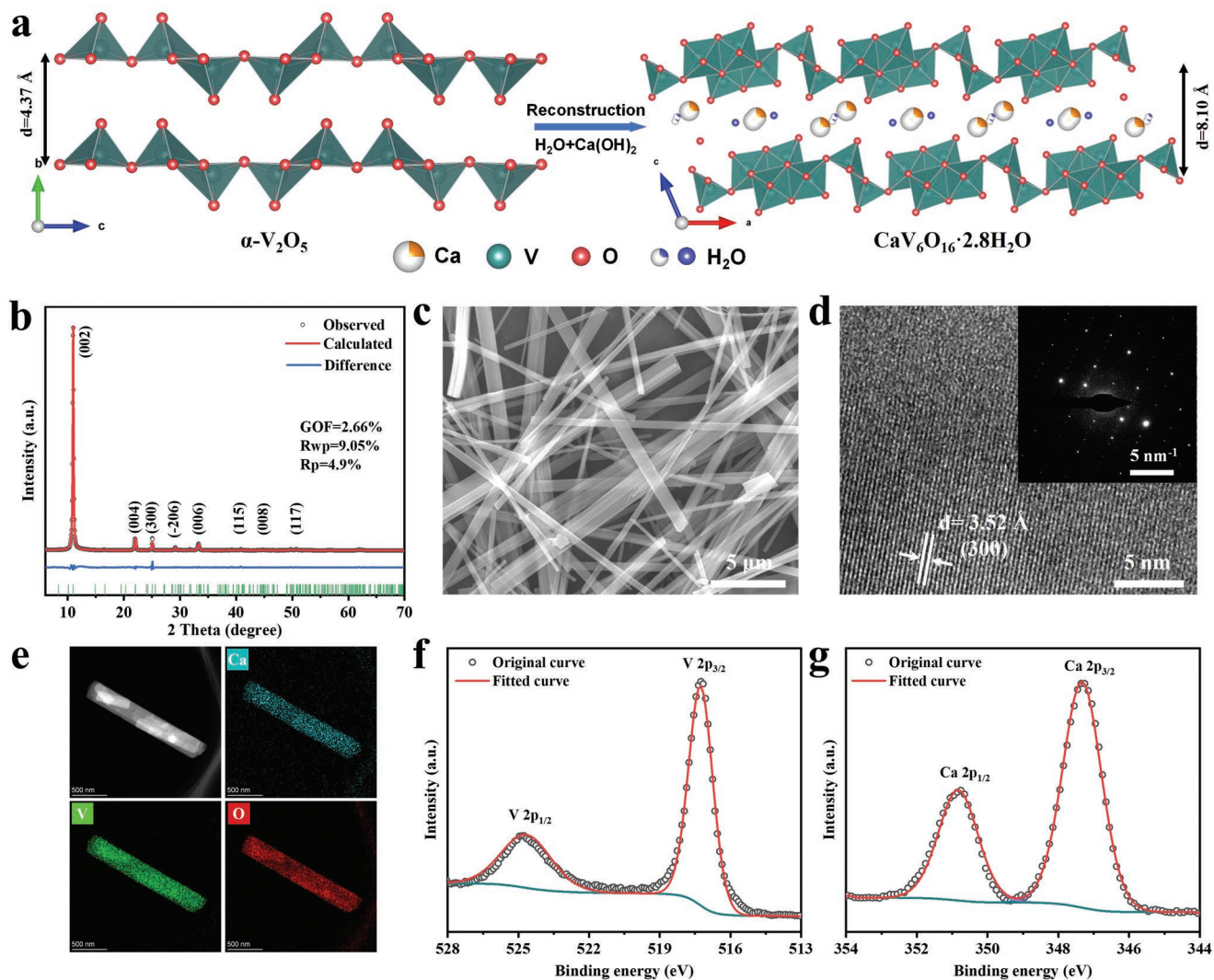


Figure 1. Structure and characterization of $CaV_6O_{16} \cdot 2.8H_2O$. a) Schematic diagram of the formation and crystal structure of CVO. b) XRD pattern and Rietveld refinement of CVO and c) SEM image of CVO. d) HRTEM image and the inset is SAED pattern. e) HAADF image and corresponding elemental maps. XPS spectra of f) V 2p and g) Ca 2p.

structure of vanadium oxide. The XRD pattern of the prepared CVO is shown in Figure 1b, and the Rietveld refinement result demonstrates that the prepared sample is metahe-wettite $\text{CaV}_6\text{O}_{16} \cdot 3\text{H}_2\text{O}$ (PDF#: 00-33-317) with the large interlayer spacing of 8.10 Å. The corresponding atomic parameters are shown in Table S1. Thermogravimetric analysis (TGA) indicates that the weight loss of the prepared CVO between 35 °C and 400 °C is 774%, corresponding to 2.8 H_2O molecules per CVO (Figure S1, Supporting Information). Scanning electron microscope (SEM) image indicates that the morphology of CVO is nanoribbons (Figure 1c). The high-resolution transmission electron microscope (HRTEM) image of CVO demonstrates the existence of defined lattice fringes with an interplanar spacing of 3.52 Å, corresponding to the (300) crystal plane of CVO (Figure 1d). The inset in Figure 1d is the selected area electron diffraction (SAED) pattern of CVO, which shows the single crystal characteristics of CVO nanoribbons. The elemental maps (Figure 1e) indicate the even distribution of Ca, V, and O in CVO nanoribbons, and the corresponding energy dispersive X-ray (EDX) spectrum further demonstrates the existence of Ca, V, and O in Figure S2, Supporting Information. XPS characterizations were used to explore the chemical state of CVO. The V 2p XPS spectrum (Figure 1f) shows that the valence state of V in CVO is +5 with the binding energy of 517.27 eV, and the Ca 2p XPS spectrum demonstrates the existence of Ca^{2+} (Figure 1g). The survey XPS spectrum of CVO reveals the existence of Ca, V, and O (Figure S3, Supporting Information). Moreover, the FTIR spectrum of CVO is shown in Figure S4, Supporting Information. The peak at 710 cm^{-1} is assigned to the V–O–V stretching mode, and the peaks at 960 and 997 cm^{-1} are attributed to the V=O stretching of $[\text{VO}_6]$ octahedron and the V=O stretching of $[\text{VO}_5]$ square pyramid, respectively.^[22] The peaks at 1617 cm^{-1} and 3428 cm^{-1} correspond to the vibrations of H_2O molecules and H–O–H bonds, respectively.^[23] The above results indicate that the metahe-wettite $\text{CaV}_6\text{O}_{16} \cdot 2.8\text{H}_2\text{O}$ with V^{5+} , large layer spacing, and the Ca^{2+} and H_2O co-pillared are obtained by the one-step hydrothermal method.

The Ca^{2+} storage performance of CVO was studied in $\text{Ca}(\text{TFSI})_2/(\text{ethylene glycol dimethyl ether})$ DME or G2 for the first time. Since Ca metal is easily passivated in these electrolytes, using Ca metal as anode will affect the evaluation of the Ca^{2+} storage performance of cathode material. As shown in Figure S5, Supporting Information, the capacity of a battery with CVO cathode, $\text{Ca}(\text{TFSI})_2$ -based electrolyte, and Ca metal anode is only $\approx 10 \text{ mAh g}^{-1}$ for the first discharge and quickly decays to $\approx 1 \text{ mAh g}^{-1}$ after 10 cycles. Activated carbon cloth (ACC) has a stable potential (3.168 V versus Ca^{2+}/Ca) during charge/discharge in $\text{Ca}(\text{TFSI})_2/\text{ether}$ -based electrolyte.^[24] Therefore, this study used ACC as a counter electrode. CVO shows a discharge capacity of 188 mAh g^{-1} at 50 mA g^{-1} in $\text{Ca}(\text{TFSI})_2/\text{DME}$ (Figure S6, Supporting Information). However, the capacity retention of CVO is only 42.2% after 90 cycles in $\text{Ca}(\text{TFSI})_2/\text{DME}$ (Figure S7, Supporting Information). When the coin cell with $\text{Ca}(\text{TFSI})_2/\text{DME}$ electrolyte was disassembled, the color change of the separator was observed (Figure S8, Supporting Information), which may be the cause of the dissolution of CVO or the side reaction of the electrolyte. However, the color change of the separator has not been observed in $\text{Ca}(\text{TFSI})_2/\text{G2}$ (Figure S9, Supporting Information). Therefore, the Ca^{2+} storage performance

of CVO is then evaluated in $\text{Ca}(\text{TFSI})_2/\text{G2}$. Figure 2a shows the charge/discharge curves of CVO with $\text{Ca}(\text{TFSI})_2/\text{G2}$ at 50 °C. CVO shows a discharge capacity of 175 mAh g^{-1} at 50 mA g^{-1} . CVO delivers the capacity retention of 75% with $\text{Ca}(\text{TFSI})_2/\text{G2}$ after 100 cycles at 50 mA g^{-1} (Figure 2b). The decrease in capacity may be caused by the escape of H_2O molecules between layers during the deep charge/discharge cycle. The long-term cycling stability of CVO is evaluated at 500 mA g^{-1} , and CVO shows a specific discharge capacity of $\approx 70 \text{ mAh g}^{-1}$ ($\approx 8 \text{ min}$ per charge/discharge) and a long cycle life of 1000 cycles with a high capacity retention of $\approx 93\%$ in $\text{Ca}(\text{TFSI})_2/\text{G2}$ (Figure 2c). Figure 2d,e shows the rate performance of CVO. CVO delivers the discharge capacity of 170.8, 134.7, 104.0, 65.0, and 47.7 mAh g^{-1} at 50, 100, 200, 500, and 800 mA g^{-1} , respectively. Even if the current density is increased to 1000 mA g^{-1} , CVO still exhibits a discharge capacity of 41.2 mAh g^{-1} . In addition, the Ca^{2+} storage performance of CVO was evaluated with $\text{Ca}(\text{TFSI})_2/\text{G2}$ at room temperature (Figure S10, Supporting Information). The charge/discharge curve of CVO under room temperature is shown in Figure S10a, Supporting Information, and CVO shows a discharge capacity of 131.7 mAh g^{-1} at 50 mA g^{-1} . After 30 cycles, CVO can still maintain a discharge capacity of 120.3 mAh g^{-1} (Figure S10b, Supporting Information). The highest discharge capacity of CVO at 500 mA g^{-1} is 44.9 mAh g^{-1} and the discharge capacity of 42.4 mAh g^{-1} can be maintained after 1000 cycles (Figure S10c, Supporting Information), which indicates that CVO has good cycling stability at high current density and room temperature. Compared with the reported inorganic cathode materials for CIBs in organic electrolytes (Table S2, Supporting Information), CVO exhibits excellent cycling performance, rate performance, and high discharge capacity. In order to study the effect of interlayer H_2O molecules on the Ca^{2+} storage performance of CVO, the CVO was treated at 250, 300, 320, 340, 360, 380, and 400 °C for 4 h under an air atmosphere (denoted as CVO-250, 300, 320, 340, 360, 380, and 400). The XRD patterns of CVO treated at different temperatures are shown in Figure S11, Supporting Information, the results show that with the increase of temperature, the interlayer spacing gradually decreases, which corresponds to the extraction of H_2O molecules from the CVO. In addition, when the temperature increased from 250 to 340 °C, the diffraction peaks intensity of $\text{Ca}_{0.5}\text{V}_3\text{O}_8$ gradually increased. When the temperature continued to increase, the diffraction peaks intensity of $\text{Ca}_{0.5}\text{V}_3\text{O}_8$ gradually weakened, while the diffraction peaks intensity of V_2O_5 and CaV_2O_6 gradually increased. Figure S12, Supporting Information, shows that the color of the sample changes from dark red to earthy yellow. Therefore, as a control, the Ca^{2+} storage performance of CVO-340 was tested at 50 °C. The Ca^{2+} storage performances of CVO-340 are shown in Figure 2a,b,c. Compared with CVO, CVO-340 exhibits low Ca^{2+} storage capacity (105.7 mAh g^{-1} @50 mA g^{-1} and 37.7 mAh g^{-1} @500 mA g^{-1}), the result demonstrates that the water lubrication may play an important role in achieving high Ca^{2+} storage capacity. In order to prove the feasibility of CVO based on Ca metal as the anode, the Ca^{2+} storage performance of CVO is evaluated with $\text{Ca}[\text{B}(\text{hfp})_4]_2/\text{DME}$ as the electrolyte and Ca metal as the anode. As shown in Figure 2f, CVO shows an initial discharge capacity of 83.4 mAh g^{-1} at 50 mA g^{-1} . However, the discharge capacity of CVO decays to 43 mAh g^{-1}

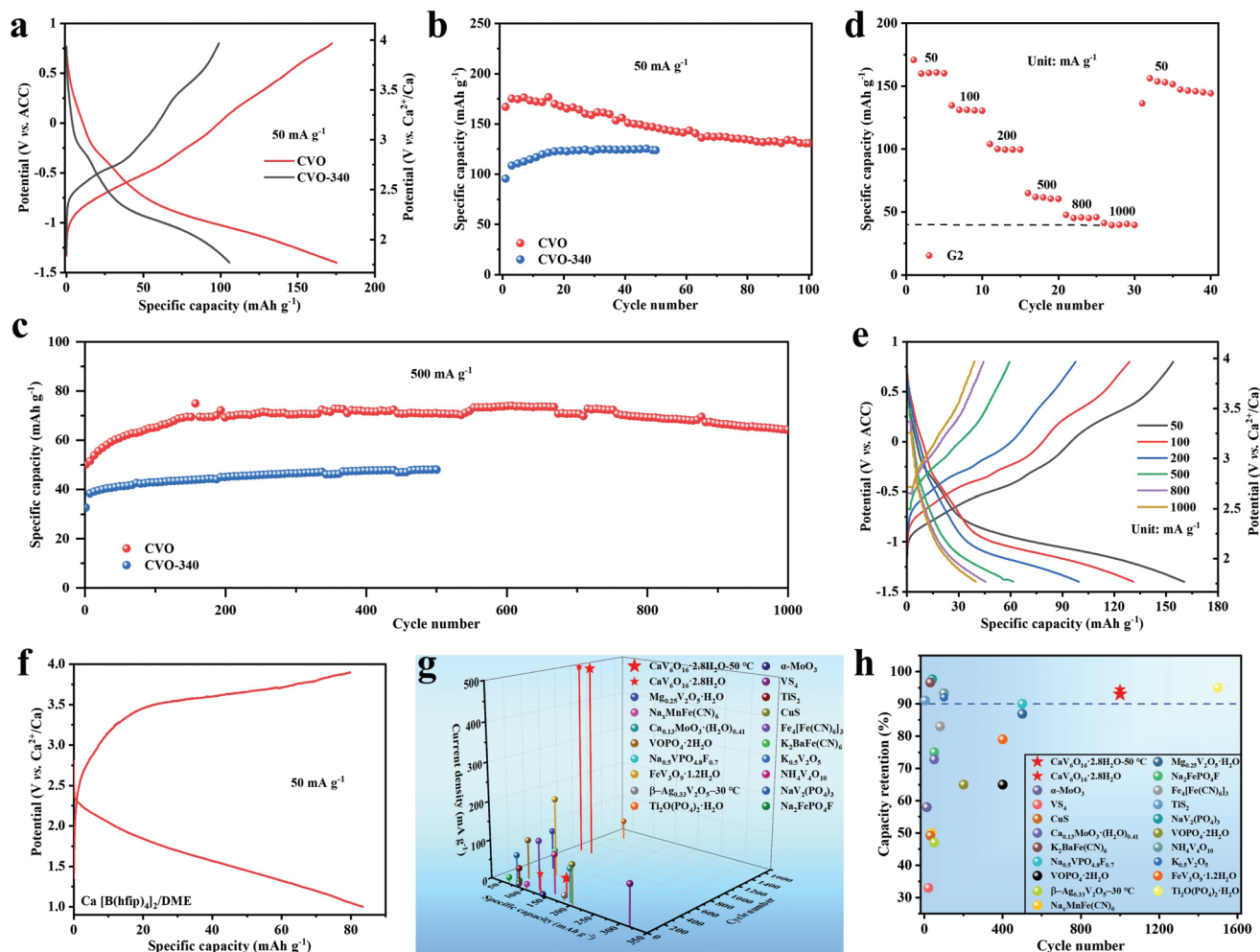


Figure 2. Calcium storage performance of $\text{CaV}_6\text{O}_{16}\cdot 2.8\text{H}_2\text{O}$. a) Galvanostatic charge/discharge profiles and b) cycling performances of CVO and CVO-340 with $\text{Ca}(\text{TFSI})_2/\text{G2}$ at 50 mA g^{-1} and 50°C . c) Long cycling performance of CVO and CVO-340 with $\text{Ca}(\text{TFSI})_2/\text{G2}$ at 500 mA g^{-1} and 50°C . d) Rate performance of CVO with $\text{Ca}(\text{TFSI})_2/\text{G2}$ at 50°C and e) corresponding charge and discharge profiles at different current densities. f) The charge/discharge curve of CVO with $\text{Ca}[\text{B}(\text{hfip})_4]_2/\text{DME}$ electrolyte at 50 mA g^{-1} and room temperature. g,h) Compare the Ca^{2+} storage performance of CVO with the reported inorganic materials for CIBs in organic electrolytes.^[3,14,15,17,18,21,25–36]

after 10 cycles (Figure S13, Supporting Information), which may be caused by the instability of the electrolyte or the passivation of the metal Ca surface.^[3,29] In addition, we compare the Ca^{2+} storage performance of CVO with the reported inorganic cathode materials for CIBs in organic electrolyte (as shown in Figure 2g,h), including cycle number, specific capacity, current density, and capacity retention. The results indicate that CVO has a long cycle life, the best rate performance (Figure 2g), and high capacity retention (>90% for 1000 cycles, Figure 2h), which indicates that CVO is an excellent cathode material for CIBs.

Multi-scan rate cyclic voltammetry (CV) is adopted to discuss the reaction kinetics of CVO (Figure 3a). The correlation between peak current and scan rate is analyzed according to Equation 1.^[37]

$$i = av^b \quad (1)$$

where a and b are adjustable parameters, i is peak current, and v is scan rate. $b = 1$ means capacitive controlled charge storage,

and $b = 0.5$ indicates diffusion dominated charge storage.^[37] The value of b can be obtained by linear fitting $\log(i)$ versus $\log(v)$. After fitting (Figure 3b), the b values of peak 1, peak 2, and peak 3 are 0.75, 0.79, and 0.72, respectively, which indicates the coexistence of capacitive control and diffusion dominated charge storage. In order to analyze the proportion of capacitive contribution at different scan rates, the proportion of capacitive contribution was calculated according to Equation 2:^[38]

$$i = k_1 v + k_2 v^{1/2} \quad (2)$$

where $k_1 v$ and $k_2 v^{1/2}$ correspond to the capacitive-controlled and diffusion-controlled responses, respectively. For example, in Figure 3c, the shaded area represents the capacitive contribution to charge storage and the proportion is 60.1%. The percentage of the diffusion-controlled and capacitive contribution at different scan rates were calculated and shown in Figure 3d. The percentage of capacitive contribution increases from 9.8% to 60.1% with the scan rate increases, indicating that the

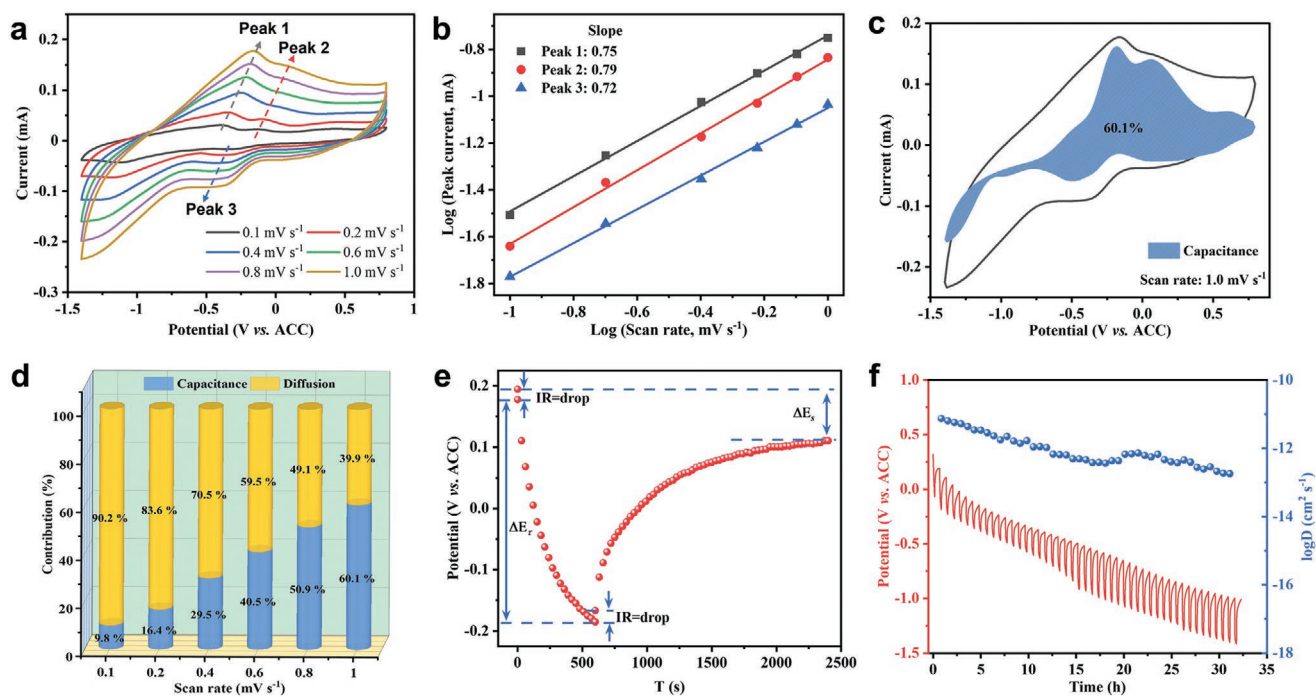


Figure 3. Reaction kinetic analysis of $\text{CaV}_6\text{O}_{16}\cdot 2.8\text{H}_2\text{O}$. a) The CV curves of CVO at different scan rates. b) $\log(i)$ versus $\log(v)$ plots of three redox peaks in CV curves. c) The calculated capacitive contribution to the charge storage of CVO at 1.0 mV s^{-1} . d) Percentage of the diffusion and capacitance contribution at different scan rates. e) GITT potential response curve of CVO with time, and the test was carried out at a constant current pulse of 30 mA g^{-1} for 10 min and a relaxation period of 30 min. f) GITT curve of CVO electrode and diffusivity versus state of discharge.

capacitive controlled charge storage becomes dominant as the scan rate increases, which makes CVO have excellent rate performance. The Ca^{2+} diffusion kinetics in the CVO was studied by galvanostatic intermittent titration technique (GITT). The Ca^{2+} diffusion coefficients (D^{GITT}) can be calculated according to Equation 3:^[39]

$$D^{\text{GITT}} = \frac{4}{\pi\tau} \left(\frac{m_B V_M}{M_B S} \right)^2 \left(\frac{\Delta E_s}{\Delta E_\tau} \right)^2 \quad (3)$$

As shown in Figure 3e, the ΔE_τ is the potential change during a constant current pulse, and the ΔE_s is the potential difference during the open circuit period. The D^{GITT} ($\text{cm}^2 \text{ s}^{-1}$) is Ca^{2+} diffusion rate, and m_B , M_B , V_M , τ , S are the mass, molar mass, the molar volume of CVO, constant current pulse time, area of the CVO electrode, respectively. The results of the GITT test are shown in Figure 3f, and CVO delivers a discharge capacity of 236.5 mAh g^{-1} , which is close to the theoretical capacity of CVO (232.4 mAh g^{-1}) with the complete transformation of V^{5+} to V^{4+} . The diffusion rate of Ca^{2+} in the CVO electrode decreases from $75 \times 10^{-12} \text{ cm}^2 \text{ s}^{-1}$ to $1.8 \times 10^{-13} \text{ cm}^2 \text{ s}^{-1}$ during the discharge process and the average diffusion rate is $1.5 \times 10^{-12} \text{ cm}^2 \text{ s}^{-1}$.

In situ XRD, in situ FTIR, ex situ XPS, TEM and XRD were performed to study the Ca^{2+} storage mechanism and structural evolution of CVO during charging and discharging. The configurations of the cell for in situ XRD and in situ FTIR tests are shown in Figure S14 and S15, Supporting Information, respectively, and $\text{Ca}(\text{TFSI})_2/\text{G2}$ electrolyte is used for in situ tests. In situ XRD patterns and the corresponding charge/discharge profiles of CVO are shown in Figure 4a. The (002) and

(004) diffraction peaks of CVO gradually shift to a high angle during the discharging, indicating that the interlayer spacing of CVO reduced (from 8.10 to 7.88 \AA), which may be caused by the increased force between layers due to the insertion of Ca^{2+} . Conversely, the corresponding diffraction peaks gradually return to the initial position during the charging process, which demonstrates that CVO has good structural reversibility. In addition, the in situ XRD results indicate that the Ca^{2+} storage mechanism of CVO is single-phase solid solution reaction with small interlayer spacing changes. Ex situ XRD patterns (Figure S16, Supporting Information) show similar crystal structure changes. The XRD patterns of the fully charged CVO after different cycles are shown in Figure S17, Supporting Information. The results indicate that the layered structure of CVO is stable during the first 10 cycles, and the (002) diffraction peak broadens and slightly shifts to a higher degree after 50 cycles. The broadening and shift of the (002) diffraction peak are related to the release of interlayer H_2O molecules or the irreversible insertion of Ca^{2+} .^[15,40] In addition, TGA for CVO after 50 cycles shows that some H_2O molecules will be deinserted during cycling (Figure S18, Supporting Information). In situ FTIR technology is used to further study the structural changes of CVO during charging and discharging. In situ FTIR spectra of CVO and the corresponding charge-discharge curves are shown in Figure 4b. The absorption band ($\approx 1617 \text{ cm}^{-1}$) corresponding to the vibration of H_2O molecules has no obvious change during the cycles, which means that the change in the interlayer H_2O molecules of CVO may be weak during initial cycles, consistent with ex situ XRD results (Figure S17, Supporting Information). The absorption band ($\approx 997 \text{ cm}^{-1}$) of

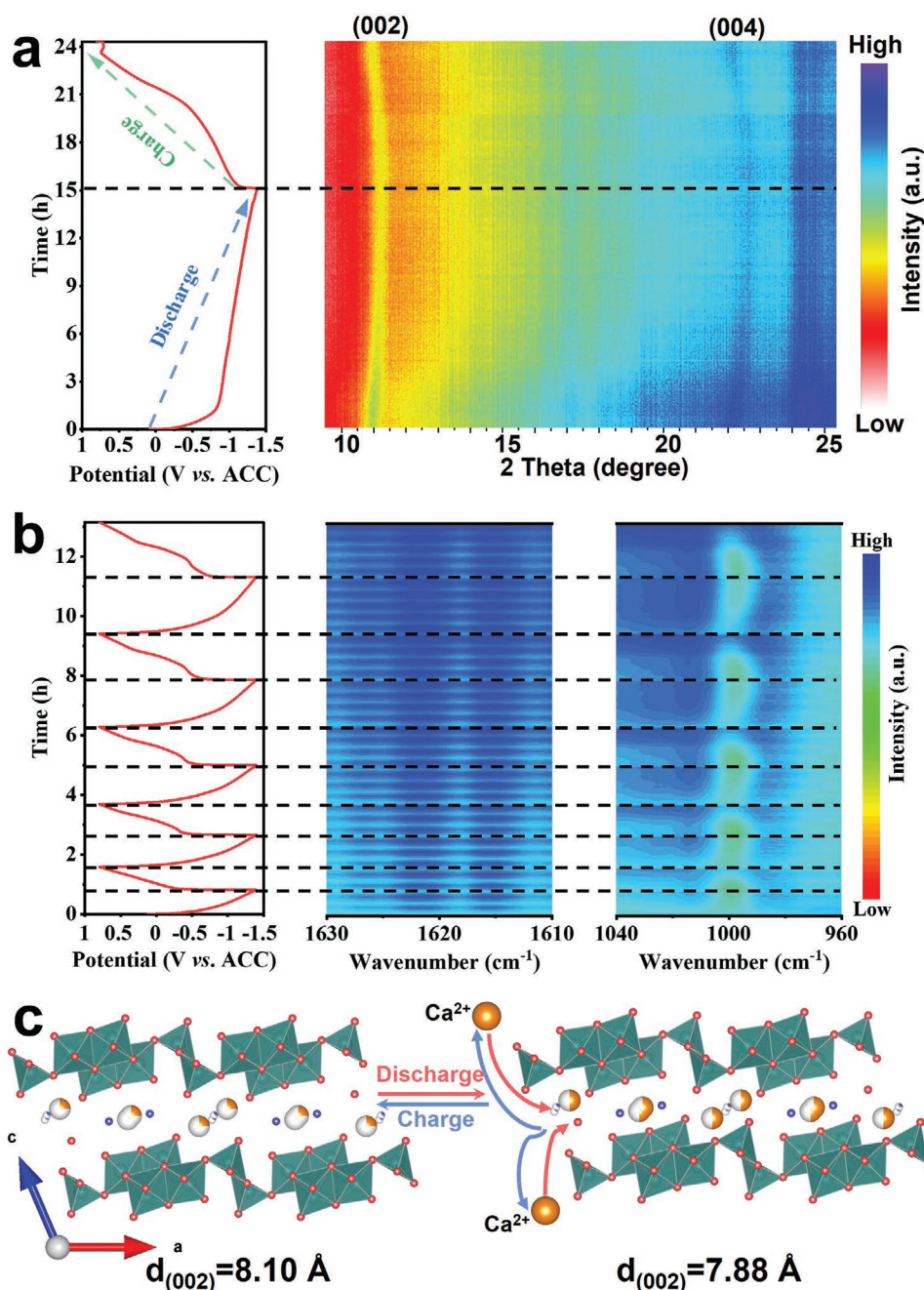


Figure 4. Calcium storage mechanism of $\text{CaV}_6\text{O}_{16} \cdot 2.8\text{H}_2\text{O}$. a) In situ XRD patterns and the corresponding charge/discharge profiles. b) In situ FTIR spectra and the corresponding charge/discharge curves. c) Schematic diagram of the Ca^{2+} storage mechanism and layer spacing changes of CVO.

V=O stretching attributed to $[\text{VO}_6]$ octahedron is red-shift and gradually increases during discharging, which is caused by the reduction of V^{5+} due to the insertion of Ca^{2+} .^[23,41] During the charging process, the absorption peak undergoes opposite changes, including intensity weakening and blue shift, which suggests that the insertion and deinsertion processes of Ca^{2+} are reversible. The Ca^{2+} storage mechanism and the change of interlayer spacing of CVO are briefly illustrated in Figure 4c. During the discharging process, Ca^{2+} ions are inserted into the interlayer of CVO, and a single-phase solid solution reaction

occurs. The interlayer spacing of CVO is reduced from 8.10 \AA to 7.88 \AA due to the strong interaction between Ca^{2+} and interlayer oxygen atoms. During the charging process, Ca^{2+} ions are released from the interlayer, and the interlayer spacing of CVO returns to the initial state (from 7.88 \AA to 8.10 \AA), which indicates that the CVO has good structural reversibility.

Ex situ XPS proved the insertion of Ca^{2+} and the change of valence state of V. The high-resolution XPS spectra of Ca 2p for CVO at different states are shown in Figure 5a. Compared with the initial state, the peak intensity of Ca 2p is significantly

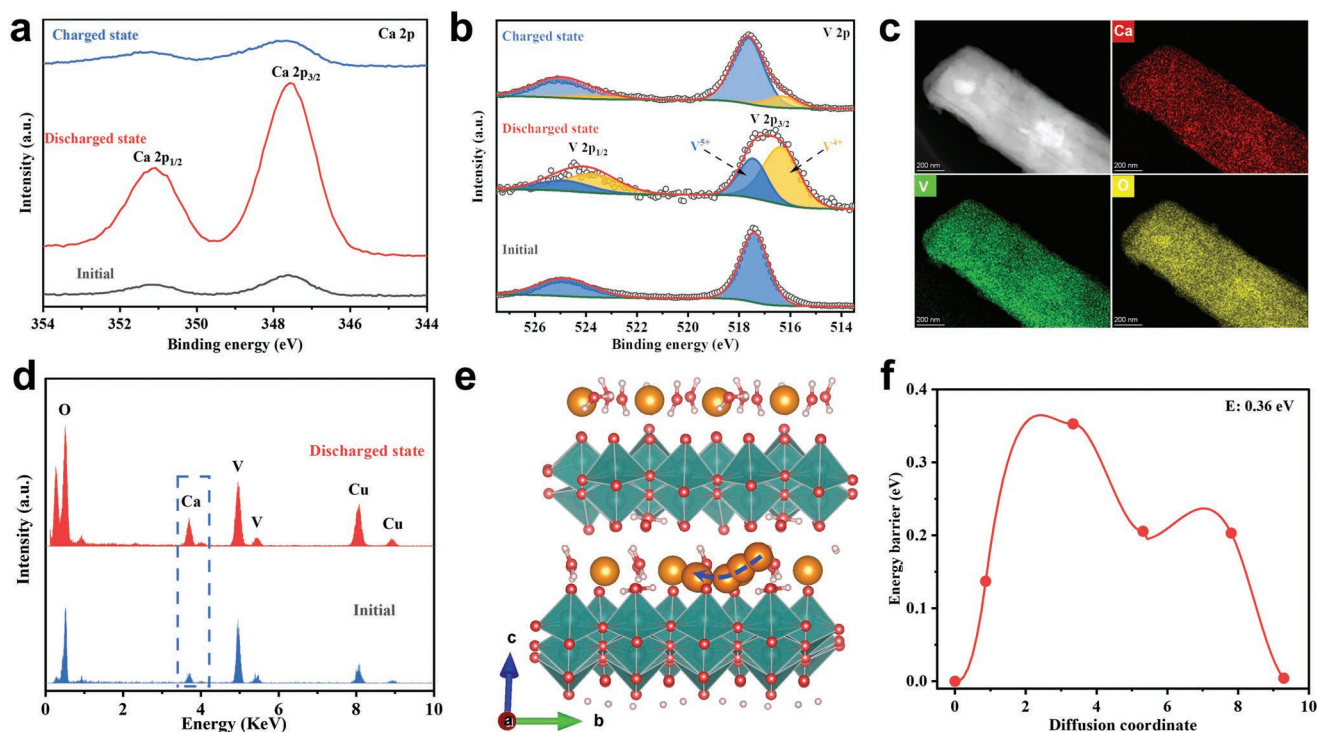


Figure 5. Calcium storage mechanism of $\text{CaV}_6\text{O}_{16}\cdot 2.8\text{H}_2\text{O}$. Ex situ XPS spectra of a) Ca 2p and b) V 2p for CVO at different states. c) HAADF image and corresponding elemental maps for the fully discharged CVO. d) EDX spectra of CVO at initial and discharged states. Diffusion path e) and corresponding diffusion energy barrier f) profiles of Ca^{2+} along the b direction in CVO.

enhanced at the discharged CVO, demonstrating that Ca^{2+} ions are inserted into CVO. The signal of Ca 2p becomes weak at the charged state, which means Ca^{2+} ions are deinserted from CVO. The XPS spectra of V 2p (Figure 5b) demonstrate that the V^{5+} is partially reduced to V^{4+} at the discharged state, which is consistent with the actual discharge capacity of CVO being less than the theoretical capacity which V^{5+} is completely reduced to V^{4+} . Most of V^{4+} is oxidized to V^{5+} at the charged state. The existence of a small amount of V^{4+} may be due to the partial residual of inserted Ca^{2+} . The HAADF image of CVO and the corresponding elemental maps at the discharged state demonstrate the even distribution of Ca, V, and O elements (Figure 5c). The EDX spectra of CVO at different states (Figure 5d) show that the signal of the Ca element is significantly enhanced at the discharged state, which further proves the insertion of Ca^{2+} . The quantitative elemental ratios for initial and discharged states are shown in Figures S19 and S20, Supporting Information. The atomic ratio of Ca and V at initial state is 0.96:6, which is close to 1:6 in CVO. The atomic ratio of Ca and V at discharged state is 2.88:6, which means that 1.92 mol Ca^{2+} may be inserted into 1.0 mol CVO corresponding to the specific capacity of 157 mAh g^{-1} . The Ca^{2+} insertion sites in CVO were analyzed by DFT computations, and the results are shown in Table S3, Supporting Information and Figure S21, Supporting Information. When site 1, site 3, or site 4 is occupied by one Ca^{2+} , the structure of CVO has similar stability and small volume change among the 4 sites analyzed. Therefore, Ca^{2+} may occupy site 1, site 3, or site 4, and the crystal structure of CVO with site 1 occupied is shown in Figure S21a, Supporting Information. When two or three Ca^{2+} inserted into CVO, the results indicate

that two Ca^{2+} may occupy site 1 and site 4, respectively, and three Ca^{2+} may occupy site 1, site 3, and site 4, respectively. The crystal structures of CVO with two Ca^{2+} inserted and three Ca^{2+} inserted are shown in Figure S21b,c, Supporting Information, respectively. The coordination environment of the inserted Ca atom is shown in Figure S21d, Supporting Information. In addition, diffusion paths of Ca^{2+} in CVO were studied by DFT computations. The three possible Ca^{2+} diffusion paths and corresponding diffusion energy barriers were optimized by nudged elastic band (NEB) method.^[42] The diffusion path profiles along the a , b , and c directions are shown in Figures S22a, and S23a, Supporting Information, and corresponding diffusion energy barriers are 14.81 eV (Figure S22b, Supporting Information), 0.36 eV (Figure 5e), and 5.91 eV (Figure S23b, Supporting Information), respectively. The results indicate that the diffusion path of Ca^{2+} along the b direction has the lowest energy barrier, which means that Ca^{2+} tends to diffuse along the b direction in CVO.

3. Conclusions

In this study, metaheawettite $\text{CaV}_6\text{O}_{16}\cdot 2.8\text{H}_2\text{O}$ was prepared and evaluated as a cathode material for CIBs. CVO shows a high discharge capacity of 175.0 mAh g^{-1} , the highest rate performance ($41.2 \text{ mAh g}^{-1}@1000 \text{ mA g}^{-1}$) and an ultra-long cycle life of 1000 cycles due to the large interlayer spacing, water lubrication, and pillar effect of Ca^{2+} . Even if Ca metal is used as the anode, CVO still delivers a discharge capacity of 83.4 mAh g^{-1} . In addition, based on the in situ XRD, in situ FTIR, and ex situ

XPS, the Ca²⁺ storage mechanism of CVO is demonstrated as a single-phase insertion/extraction reaction with good structural stability and reversibility. DFT computations indicate that Ca²⁺ tends to diffuse along the *b* direction with low energy barrier of 0.36 eV in CVO. This work points out a new direction for developing excellent performance cathode materials for CIBs.

Supporting Information

Supporting Information is available from the Wiley Online Library or from the author.

Acknowledgements

J.W. and J.W. contributed equally to this work. This work was supported by the National Natural Science Foundation of China (52172231, 51832004, U1804253, 51972259), the Foshan Xianhu Laboratory of the Advanced Energy Science and Technology Guangdong Laboratory (XHT2020-003), Sanya Science and Education Innovation Park of Wuhan University of Technology (2020KF0015), the Fundamental Research Funds for the Central Universities (WUT: 2021-024GX, 2021III001GL).

Conflict of Interest

The authors declare no conflict of interest.

Data Availability Statement

The data that support the findings of this study are available from the corresponding author upon reasonable request.

Keywords

Ca-ion batteries, CaV₆O₁₆·2.8H₂O, in situ FTIR, layered vanadium oxides, multivalent-ion batteries

Received: January 19, 2022

Revised: March 15, 2022

Published online:

- [1] M. Mao, T. Gao, S. Hou, C. Wang, *Chem. Soc. Rev.* **2018**, *47*, 8804.
- [2] M. E. Arroyo-de Dompablo, A. Ponrouch, P. Johansson, M. R. Palacin, *Chem. Rev.* **2019**, *120*, 6331.
- [3] Z. L. Xu, J. Park, J. Wang, H. Moon, G. Yoon, J. Lim, Y. J. Ko, S. P. Cho, S. Y. Lee, K. Kang, *Nat. Commun.* **2021**, *12*, 3369.
- [4] S. D. Pu, C. Gong, X. Gao, Z. Ning, S. Yang, J.-J. Marie, B. Liu, R. A. House, G. O. Hartley, J. Luo, P. G. Bruce, A. W. Robertson, *ACS Energy Lett.* **2020**, *5*, 2283.
- [5] I. D. Hosein, *ACS Energy Lett.* **2021**, *6*, 1560.
- [6] B. Ji, H. He, W. Yao, Y. Tang, *Adv. Mater.* **2020**, *33*, 2005501.
- [7] Z. Li, O. Fuhr, M. Fichtner, Z. Zhao-Karger, *Energy Environ. Sci.* **2019**, *12*, 3496.
- [8] A. Shyamsunder, L. E. Blanc, A. Assoud, L. F. Nazar, *ACS Energy Lett.* **2019**, *4*, 2271.
- [9] M. Wang, C. Jiang, S. Zhang, X. Song, Y. Tang, H. M. Cheng, *Nat. Chem.* **2018**, *10*, 667.
- [10] J. Park, Z. L. Xu, G. Yoon, S. K. Park, J. Wang, H. Hyun, H. Park, J. Lim, Y. J. Ko, Y. S. Yun, K. Kang, *Adv. Mater.* **2020**, *32*, 1904411.
- [11] S. J. Richard Prabakar, A. B. Ikhe, W. B. Park, K. C. Chung, H. Park, K. J. Kim, D. Ahn, J. S. Kwak, K. S. Sohn, M. Pyo, *Adv. Sci.* **2019**, *6*, 1902129.
- [12] T. Tojo, Y. Sugiura, R. Inada, Y. Sakurai, *Electrochim. Acta* **2016**, *207*, 22.
- [13] T. Shiga, H. Kondo, Y. Kato, M. Inoue, *J. Phys. Chem. C* **2015**, *119*, 27946.
- [14] S. Kim, L. Yin, M. H. Lee, P. Parajuli, L. Blanc, T. T. Fister, H. Park, B. J. Kwon, B. J. Ingram, P. Zapol, R. F. Klie, K. Kang, L. F. Nazar, S. H. Lapidus, J. T. Vaughey, *ACS Energy Lett.* **2020**, *5*, 3203.
- [15] J. Wang, S. Tan, F. Xiong, R. Yu, P. Wu, L. Cui, Q. An, *Chem. Commun.* **2020**, *56*, 3805.
- [16] B. Jeon, J. W. Heo, J. Hyoung, H. H. Kwak, D. M. Lee, S.-T. Hong, *Chem. Mater.* **2020**, *32*, 8772.
- [17] M. S. Chae, H. H. Kwak, S.-T. Hong, *ACS Appl. Energy Mater.* **2020**, *3*, 5107.
- [18] W. Ren, F. Xiong, Y. Fan, Y. Xiong, Z. Jian, *ACS Appl. Mater. Interfaces* **2020**, *12*, 10471.
- [19] Y. Murata, S. Takada, T. Obata, T. Tojo, R. Inada, Y. Sakurai, *Electrochim. Acta* **2019**, *294*, 210.
- [20] Y. Zhao, C. Han, J. Yang, J. Su, X. Xu, S. Li, L. Xu, R. Fang, H. Jiang, X. Zou, B. Song, L. Mai, Q. Zhang, *Nano Lett.* **2015**, *15*, 2180.
- [21] X. Xu, M. Duan, Y. Yue, Q. Li, X. Zhang, L. Wu, P. Wu, B. Song, L. Mai, *ACS Energy Lett.* **2019**, *4*, 1328.
- [22] N. Wang, W. Chen, L. Mai, Y. Dai, *J. Solid State Chem.* **2008**, *181*, 652.
- [23] H. Tang, N. Xu, C. Pei, F. Xiong, S. Tan, W. Luo, Q. An, L. Mai, *ACS Appl. Mater. Interfaces* **2017**, *9*, 28667.
- [24] X. Liu, G. A. Elia, S. Passerini, *J. Power Sources Adv.* **2020**, *2*, 100008.
- [25] A. L. Lipson, B. Pan, S. H. Lapidus, C. Liao, J. T. Vaughey, B. J. Ingram, *Chem. Mater.* **2015**, *27*, 8442.
- [26] A. L. Lipson, S. Kim, B. Pan, C. Liao, T. T. Fister, B. J. Ingram, *J. Power Sources* **2017**, *369*, 133.
- [27] M. Cabello, F. Nacimiento, R. Alcántara, P. Lavela, C. Pérez Vicente, J. L. Tirado, *Chem. Mater.* **2018**, *30*, 5853.
- [28] N. Kuperman, P. Padigi, G. Goncher, D. Evans, J. Thiebess, R. Solanki, *J. Power Sources* **2017**, *342*, 414.
- [29] Z. Li, B. P. Vinayan, P. Jankowski, C. Njel, A. Roy, T. Vegge, J. Maibach, J. M. G. Lastra, M. Fichtner, Z. Zhao-Karger, *Angew. Chem., Int. Ed.* **2020**, *59*, 11483.
- [30] C. Lee, Y.-T. Jeong, P. M. Nogales, H.-Y. Song, Y. Kim, R.-Z. Yin, S.-K. Jeong, *Electrochem. Commun.* **2019**, *98*, 115.
- [31] P. Padigi, G. Goncher, D. Evans, R. Solanki, *J. Power Sources* **2015**, *273*, 460.
- [32] M. E. Purbarani, J. Hyoung, S.-T. Hong, *ACS Appl. Energy Mater.* **2021**, *4*, 7487.
- [33] T. N. Vo, H. Kim, J. Hur, W. Choi, I. T. Kim, *J. Mater. Chem. A* **2018**, *6*, 22645.
- [34] M. S. Chae, D. Setiawan, H. J. Kim, S.-T. Hong, *Batteries* **2021**, *7*, 54.
- [35] J. Hyoung, J. W. Heo, B. Jeon, S.-T. Hong, *J. Mater. Chem. A* **2021**, *9*, 20776.
- [36] S. J. R. Prabakar, W.-B. Park, J. Y. Seo, S. P. Singh, D. Ahn, K.-S. Sohn, M. Pyo, *Energy Storage Mater.* **2021**, *43*, 85.
- [37] V. Augustyn, J. Come, M. A. Lowe, J. W. Kim, P. L. Taberna, S. H. Tolbert, H. D. Abruna, P. Simon, B. Dunn, *Nat. Mater.* **2013**, *12*, 518.
- [38] J. Wang, J. Polleux, J. Lim, B. Dunn, *J. Phys. Chem. C* **2007**, *111*, 14925.
- [39] E. Deiss, *Electrochim. Acta* **2005**, *50*, 2927.
- [40] J. Hyoung, J. W. Heo, M. S. Chae, S. T. Hong, *ChemSusChem* **2019**, *12*, 1069.
- [41] Q. Wei, J. Liu, W. Feng, J. Sheng, X. Tian, L. He, Q. An, L. Mai, *J. Mater. Chem. A* **2015**, *3*, 8070.
- [42] G. Henkelman, B. P. Uberuaga, H. Jónsson, *J. Chem. Phys.* **2000**, *113*, 9901.